THE INFORMATION CONTENT OF MCDESPOT

By

Christopher Lynn Lankford

Thesis

Submitted to the Faculty of the

Graduate School of Vanderbilt University

in partial fulfillment of the requirements

for the degree of

MASTER OF SCIENCE

in

Biomedical Engineering

December, 2011

Nashville, Tennessee

Approved:

Mark D. Does

E. Brian Welch

ACKNOWLEDGEMENTS

I would like to acknowledge and thank the source of funding for this project, NIH grant number EB001744, and my advisor, Dr. Mark Does, who contributed liberally to the work presented herein. I acknowledge and thank Professor Emeritus Robert J. Roselli, without whose name this section would be incomplete and without whose help this thesis would not exist. I would also like to acknowledge and thank my father, Charles Lankford, for sharing the joys of engineering with me through financial and emotional support, a (thankfully) hereditary mindset, and stimulating conversations over the past few years. Lastly, I thank my friends and the rest of my family: my mother Nancy "Kay" Lankford, sister Molly, and partner Mary have all been particularly helpful.

LIST OF TABLES

LIST OF FIGURES

TABLE OF CONTENTS

Page

CHAPTER I

INTRODUCTION

I.1 Challenges Facing White Matter and Myelin Imaging

White matter, a type of brain tissue located below the cortical surface in most vertebrate cerebra, consists primarily of neuronal axons wrapped in layers of lipid membrane known as myelin sheaths. These sheaths impede ionic interactions between the axonal cytosol and the extracellular environment, inducing an increase in signal conduction velocity between the non-myelinated nodes of Ranvier distributed along the axon's length. Several clinically-relevant diseases are characterized by or coincide with a loss of myelin in white matter or other brain tissues, the most well-known of which being multiple sclerosis (1). Other diseases, such as schizophrenia, correlate instead with a destructive change in myelin structure or function rather than a degradation of myelinating cells themselves (2, 3). Due to the prevalence and severity of these diseases, inexpensive, non-invasive techniques for evaluating the extent of myelin degeneration—or more subtle changes to myelin structure—would be invaluable to the medical community.

Unfortunately, as elaborated below, the most common clinical imaging protocols are only capable of identifying macroscopic regions of demyelination such as multiple sclerotic lesions. Efforts to delve into more informative, quantitative measures of myelin structure have spurred the development of a multitude of complex magnetic resonance imaging (MRI) pulse sequences, many of which target myelin content through the unique MR transverse relaxation time (T_2) of water protons trapped between a myelin sheath's

lipid bilayers (4-12). These pulse sequences often require clinically unfeasible (i.e., hours for whole-brain coverage) scan times and provide results which are biased by non-negligible confounding factors. One recently developed protocol, the multi-component driven equilibrium single pulse observation of T_1 and T_2 (mcDESPOT), uses clinically established, fast pulse sequences to purportedly provide accurate measures of quantitative white matter parameters (12), including water residence times which may inform on myelin thickness (13, 14). An independent analysis of the method is needed before further optimization or clinical application can be realized; the following work uses the Cramer-Rao lower bound, a statistical metric computed directly from the mcDESPOT signal equation, to evaluate the intrinsic precision of parameter estimates garnered using this protocol.

I.1.1 Foundations of Conventional Myelin Imaging Techniques

Multiple sclerotic lesions (i.e., sites of extensive myelin degeneration) have been known for many years to be hyperintense on T_2-weighted scans, and T_2-weighted MRI is listed among the disease's gold standards of diagnosis (15-17). These scans typically utilize some variant of the spin-echo pulse sequence, including the "fast" spin-echo sequence (18-19), and are capable of whole-brain coverage in clinically tractable times. As a price for their elegance and ease of clinical implementation, though, T_2-weighted images are not quantitative in any relevant sense and cannot provide sub-voxel information about myelin levels. Instead, they are primarily useful for determining the size and number of lesions in patients. In order to obtain deeper understanding of a patient's myelin distribution and structure, one must consider the mechanisms behind

contrast generation more carefully and tailor pulse sequences to optimally identify those mechanisms.

Regions of low myelination are thought to appear bright on T_2-weighted images due to the short, relatively unique T_2 of water trapped between myelin membrane layers (20-25). Researchers have used this feature of myelinated tissue to quantify the fraction of myelin-associated water protons in an imaging voxel (4-12, 24, 25). One common protocol for identifying the "myelin water fraction" (MWF) follows. First, a variant of the spin-echo pulse sequence acquires multiple signal echoes between equally-spaced 180° radiofrequency (RF) refocusing pulses. After fitting the signal vs. echo time (TE) curve to a spectrum of exponential decay curves and applying constraints such as minimum spectral curvature or energy (24), the MWF is calculated as the fraction of signal contributed by fast-decaying (10 ms < T_2 < 50 ms, usually) exponentials (24, 25). While the multiple spin-echo MWF has been used with much success in a research environment, it is complicated by a need for robust RF refocusing and a limitation to two-dimensional imaging, implying impractical whole-brain scan times when each slice can take nearly half an hour to acquire. Furthermore, due to the nature of the multiple spin-echo signal equation, intercompartmental water exchange (i.e., the transfer of protons or magnetization between myelin water and intra-/extracellular water) will bias any estimates of tissue parameters such as the MWF, but cannot be explicitly accounted for in fitting algorithms (13).

Ironically, a second method of quantifying myelin content is founded on a very similar phenomenon to the source of bias in the MWF: magnetization transfer. The ratio of bound protons in a voxel (i.e., broad resonance, quickly dephasing macromolecular

protons) to the number of free protons (i.e., water protons), ideally a rough measure of myelination due to myelin's high lipid content, can be calculated using quantitative magnetization transfer (qMT) imaging (26-31). Unfortunately, the qMT-based pool size ratio is not specific to myelin-associated macromolecules and has been shown to correlate poorly with other aspects of myelin microstructure, such as myelin thickness (13).

I.2 Generalized Differential Equations for Two Relaxing Signal Compartments

I.2.1 Modeling Free Precession and Relaxation

The myelin water fraction, or the percent of signal contribution from exponentials with short time constants, can be defined through a general model of two well-mixed signal components decaying toward equilibrium with different relaxation rates. Examine the single-compartment Bloch equations describing relaxation and precession in the laboratory frame in the absence of a B_1 field (32):

$$\frac{\partial M_x}{\partial t} = -\frac{M_x}{T_2} - \omega M_y \qquad \textbf{(1.1)}$$

$$\frac{\partial M_y}{\partial t} = \omega M_x - \frac{M_y}{T_2} \qquad \textbf{(1.2)}$$

$$\frac{\partial M_z}{\partial t} = -\frac{(M_z - M_0)}{T_1}, \qquad \textbf{(1.3)}$$

where the magnetization vector $\mathbf{M} = \begin{bmatrix} M_x & M_y & M_z \end{bmatrix}^T$ (with the symbol ^{T} being the matrix transpose) is relaxing with a transverse relaxation rate $R_2 = 1/T_2$ and a longitudinal relaxation rate $R_1 = 1/T_1$ toward an equilibrium state $\mathbf{M_0} = \begin{bmatrix} 0 & 0 & M_0 \end{bmatrix}^T$. The magnetization vector is simultaneously precessing about an external magnetic field (i.e., the *z*-axis) at an angular velocity defined by the Larmor equation:

$$\omega = -\gamma B_z . \quad \textbf{(2)}$$

In this equation, B_z is the summed strength of the main and gradient magnetic fields, and γ is the gyromagnetic ratio of a proton, equal to 267.522 million radians per second per tesla (33). Shifting to a frame of reference which rotates in the *x*-*y* plane at the Larmor frequency corresponding to the main magnet strength results in the coupled differential equations

$$\frac{\partial M'_x}{\partial t} = -\frac{M'_x}{T_2} + \Delta\omega M'_y \quad \textbf{(3.1)}$$

$$\frac{\partial M'_y}{\partial t} = -\Delta\omega M'_x - \frac{M'_y}{T_2} \quad \textbf{(3.2)}$$

$$\frac{\partial M_z}{\partial t} = -\frac{(M_z - M_0)}{T_1}, \quad \textbf{(3.3)}$$

where the relative (clockwise) frequency $\Delta\omega$ is equal to $-(\omega - \gamma B_0)$, such that $\Delta\omega$ is greater than zero when precession relative to γB_0 occurs more quickly in the clockwise direction and is less than zero when precession lags behind the rotating reference frame. Readers should note that the main magnetic field B_0 has been assumed to lie in the positive *z* direction.

I.2.2 Extension to Two Exchanging Compartments

In the simplest case of two-component relaxation, the signal at any time *t* is a weighted sum of the signals of the individual components. For example,

$$M(t) = f_S M_S(t) + f_F M_F(t), \quad \textbf{(4)}$$

where S and F represent the slow- and fast-relaxing compartments, respectively, and *f* is a fraction of the voxel volume occupied by each well-mixed compartment. Some authors (9,

34, others) elect to use separate values for equilibrium magnetization (M_0) in each compartment rather than multiply the signal in each compartment by its respective volume fraction; it can be plainly seen that these approaches are equivalent.

In order to remain open to the possibility of exchange between the slow- and fast-decaying compartments, which has been concluded to be non-negligible in some myelinated tissues (13, 14), Eq. 3 must be rewritten to include cross-compartment terms (35):

$$\frac{\partial M_{x,\mathrm{F}}}{\partial t} = -\frac{M_{x,\mathrm{F}}}{T_{2,\mathrm{F}}} + \Delta\omega M_{y,\mathrm{F}} - k_{\mathrm{FS}} M_{x,\mathrm{F}} + k_{\mathrm{SF}} M_{x,\mathrm{S}} \quad \textbf{(5.1)}$$

$$\frac{\partial M_{x,\mathrm{S}}}{\partial t} = -\frac{M_{x,\mathrm{S}}}{T_{2,\mathrm{S}}} + \Delta\omega M_{y,\mathrm{S}} - k_{\mathrm{SF}} M_{x,\mathrm{S}} + k_{\mathrm{FS}} M_{x,\mathrm{F}} \quad \textbf{(5.2)}$$

$$\frac{\partial M_{y,\mathrm{F}}}{\partial t} = -\Delta\omega M_{x,\mathrm{F}} - \frac{M_{y,\mathrm{F}}}{T_{2,\mathrm{F}}} - k_{\mathrm{FS}} M_{y,\mathrm{F}} + k_{\mathrm{SF}} M_{y,\mathrm{S}} \quad \textbf{(5.3)}$$

$$\frac{\partial M_{y,\mathrm{S}}}{\partial t} = -\Delta\omega M_{x,\mathrm{S}} - \frac{M_{y,\mathrm{S}}}{T_{2,\mathrm{S}}} - k_{\mathrm{SF}} M_{y,\mathrm{S}} + k_{\mathrm{FS}} M_{y,\mathrm{F}} \quad \textbf{(5.4)}$$

$$\frac{\partial M_{z,\mathrm{F}}}{\partial t} = -\frac{(M_{z,\mathrm{F}} - f_{\mathrm{F}} M_0)}{T_{1,\mathrm{F}}} - k_{\mathrm{FS}} M_{z,\mathrm{F}} + k_{\mathrm{SF}} M_{z,\mathrm{S}} \quad \textbf{(5.5)}$$

$$\frac{\partial M_{z,\mathrm{S}}}{\partial t} = -\frac{(M_{z,\mathrm{S}} - f_{\mathrm{S}} M_0)}{T_{1,\mathrm{S}}} - k_{\mathrm{SF}} M_{z,\mathrm{S}} + k_{\mathrm{FS}} M_{z,\mathrm{F}}. \quad \textbf{(5.6)}$$

As was the case with decay rates R_1 and R_2, exchange rates k_{FS} (fast-to-slow) and k_{SF} (slow-to-fast) can be equivalently expressed as their inverses, the "mean residence times" τ of a proton in a given water pool before migrating to the other water pool. The "prime" notation used to differentiate between the laboratory and rotating frame has been dropped in Eq. 5. Two further assumptions are usually made (12, 36-38) to reduce the dimensionality of these equations. First, the assumption that only two water pools exist in

the imaging volume, i.e. $f_F + f_S = 1$. The second assumption is that the intercompartmental exchange within the volume has reached a state of equilibrium. A mass balance assuming first-order rate kinetics reveals that the outflow rate-compartment size product (i.e., kV, with V the compartment volume) must be equal in each compartment. Dividing by the total volume results in the equation $k_{FS}f_F = k_{SF}f_S$, relating the two exchange rates.

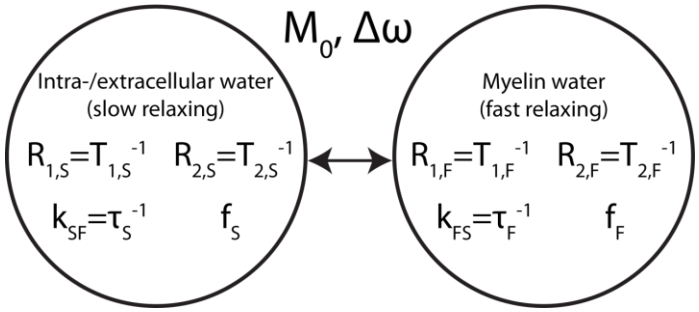

Figure 1. Two-compartment relaxation model. The ten relevant parameters of a two-compartment model are listed, along with identities for decay/exchange rates. Included parameters are transverse decay rates R_2, longitudinal decay rates R_1, exchange rates k, volume fractions f, equilibrium magnetization M_0, and off-resonance $\Delta\omega$. Common assumptions include $f_F + f_S = 1$ (only two compartments) and $f_F k_{FS} = f_S k_{SF}$ (equilibrium), reducing the number of independent parameters to eight.

Figure 1 summarizes the exchanging two-compartment model in a diagram format. It shows the four relaxation rates, two exchange rates, two signal fractions, and the total equilibrium magnetization and off-resonance term. After considering the two assumptions stated above, two of the ten listed parameters (namely, f_S and k_{SF}) can be rewritten in terms of other parameters, effectively reducing the dimensionality of any inverse problems applied to this model.

I.2.3 Expression in Matrix Form

In order to simplify upcoming calculations, a matrix form of Eq. 5 has been adopted:

$$\frac{\mathrm{d}\mathbf{M}}{\mathrm{dt}} = \mathbf{AM} + \mathbf{C}, \tag{6}$$

with

$$\mathbf{M} = \begin{bmatrix} M_{x,\mathrm{F}} \\ M_{x,\mathrm{S}} \\ M_{y,\mathrm{F}} \\ M_{y,\mathrm{S}} \\ M_{z,\mathrm{F}} \\ M_{z,\mathrm{S}} \end{bmatrix},$$

$$\mathbf{A} = \begin{bmatrix} -R_{2,\mathrm{F}} - k_{\mathrm{FS}} & k_{\mathrm{SF}} & \Delta\omega & 0 & 0 & 0 \\ k_{\mathrm{FS}} & -R_{2,\mathrm{S}} - k_{\mathrm{SF}} & 0 & \Delta\omega & 0 & 0 \\ -\Delta\omega & 0 & -R_{2,\mathrm{F}} - k_{\mathrm{FS}} & k_{\mathrm{SF}} & 0 & 0 \\ 0 & -\Delta\omega & k_{\mathrm{FS}} & -R_{2,\mathrm{S}} - k_{\mathrm{SF}} & 0 & 0 \\ 0 & 0 & 0 & 0 & -R_{1,\mathrm{F}} - k_{\mathrm{FS}} & k_{\mathrm{SF}} \\ 0 & 0 & 0 & 0 & k_{\mathrm{FS}} & -R_{1,\mathrm{S}} - k_{\mathrm{SF}} \end{bmatrix},$$

and

$$\mathbf{C} = M_0 \begin{bmatrix} 0 \\ 0 \\ 0 \\ 0 \\ R_{1,\mathrm{F}} f_{\mathrm{F}} \\ R_{1,\mathrm{S}} f_{\mathrm{S}} \end{bmatrix},$$

and as mentioned above, $R_1 = 1/T_1$, $R_2 = 1/T_2$, and the subscripts F and S represent the fast- and slow-decaying compartments respectively.

I.3 Multi-Component Driven Equilibrium Single Pulse Observation of T_1 and T_2

In order to address some of the issues surrounding myelin imaging, Deoni, et al developed a protocol which is purportedly able to achieve accurate, precise estimates for the eight independent parameters of the exchanging two-pool model (12, 38) and has since been successfully applied in infant brain (37) and cervical spinal cord (36). The multi-component driven equilibrium single pulse observation of T_1 and T_2 (mcDESPOT) not only attempts to provide a direct estimate of water exchange between myelin and intra-/extracellular water, but is also a fast, versatile, easily translatable protocol due to its simple pulse sequences: the common balanced steady-state free precession (bSSFP) and spoiled gradient echo (SPGR) sequences.

Early mcDESPOT literature proposed acquiring SPGR and SSFP images at variable flip angles, then fitting the ensemble of data to a seven-parameter model of the two-pool system (12). The model was reduced from eight to seven independent parameters by assuming no B_0 inhomogeneity ($\Delta\omega$ assumed to be on-resonance). The fitting algorithm in these early publications utilized non-Newtonian iterative methods and a least-squares cost function. A more recent variation of the mcDESPOT protocol included the off-resonance term in the fitting by acquiring twice as many SSFP images—one set using the standard 180° RF phase increment from repetition to repetition (also called "alternating" RF pulses) and the other a 0° RF phase increment. Acquiring SSFP images using both excitation phase schemes has been shown to provide high quality frequency maps in tissue when other factors are held fixed (39, 40). Recent versions of mcDESPOT have additionally used an inversion-prepared gradient echo image to measure and accommodate for B_1 inhomogeneity by using a more accurate flip angle in

the regression model (38, 41). The parametric fitting algorithm has evolved over time also, but has yet to deviate from the least-squares criterion. An overview of the two pulse sequences utilized by mcDESPOT, bSSFP and SPGR, including matrix forms of their signal equations, follows.

I.3.1 Balanced Steady-State Free Precession (bSSFP)

Balanced steady-state free precession is most commonly identified as a gradient-recalled echo sequence, meaning the magnetic field gradients are used to dephase and refocus spins in the imaging volume. (This is in contrast to a spin-echo sequence, which uses 180° RF pulses to refocus macroscopic B_0 inhomogeneity-induced spin dephasing.) In order to refocus spins, the zeroth moment (i.e., area under the curve) of the read-out gradient at every echo time must be equal to zero. Furthermore, in a "balanced" MRI pulse sequence, the zeroth moment of the gradients at the end of every repetition time (TR) is also equal to zero. Ideally, this allows for every RF pulse to affect all spins in the imaging volume identically. As this ideal scenario is difficult to achieve due to field inhomogeneities, short repetition times are used to minimize dephasing (42); the minimum TR defined by gradient and RF strength limitations is usually chosen. bSSFP pulse sequences are available on many clinical scanners and can be used for fast, 3D, or multi-slice imaging, and due to their nature as balanced sequences, generally have high signal-to-noise ratios (SNR) (40, 43, 44).

When deriving the signal equation for bSSFP, it is sufficient to find a steady-state solution for $\mathbf{M}(t = nTR^{-})$, $n \in \mathbb{Z}$, ignoring T_2^* relaxation between the acquired echo and the RF pulses. This relaxation will affect all mcDESPOT bSSFP images equally if a

constant TR (with $TE = TR/2$) is used, and can thus be integrated into an effective M_0. In order to find a steady-state solution to Eq. 6 under repeated RF excitation, it must first be solved for the interval $0 < t < TR^{-}$. Assuming the matrix **A** is invertible and the matrices **A** and **C** are not changing over the interval,

$$\frac{\mathrm{d}(\mathbf{M}+\mathbf{A}^{-1}\mathbf{C})}{\mathrm{dt}} = \mathbf{A}(\mathbf{M}+\mathbf{A}^{-1}\mathbf{C}), \tag{7}$$

which has the well-known solution

$$\begin{aligned} \mathbf{M}(t)+\mathbf{A}^{-1}\mathbf{C} &= e^{\mathbf{A}t}\left(\mathbf{M}(0^{+})+\mathbf{A}^{-1}\mathbf{C}\right) \\ \mathbf{M}(t) &= e^{\mathbf{A}t}\left(\mathbf{M}(0^{+})+\mathbf{A}^{-1}\mathbf{C}\right)-\mathbf{A}^{-1}\mathbf{C} \\ &= e^{\mathbf{A}t}\mathbf{M}(0^{+})+\left(e^{\mathbf{A}t}-\mathbf{I}\right)\mathbf{A}^{-1}\mathbf{C} \end{aligned} \tag{8}$$

where **I** is the 6x6 identity matrix and the exponential terms are the matrix exponential function. Before invoking the steady state, define an excitation rotation matrix **R** with flip angle α such that

$$\mathbf{R}(\alpha) = \begin{pmatrix} 1 & 0 & 0 & 0 & 0 & 0 \\ 0 & 1 & 0 & 0 & 0 & 0 \\ 0 & 0 & \cos(\alpha) & 0 & \sin(\alpha) & 0 \\ 0 & 0 & 0 & \cos(\alpha) & 0 & \sin(\alpha) \\ 0 & 0 & -\sin(\alpha) & 0 & \cos(\alpha) & 0 \\ 0 & 0 & 0 & -\sin(\alpha) & 0 & \cos(\alpha) \end{pmatrix}. \tag{9}$$

It should be noted that the definition in Eq. 9 assumes an instantaneous RF pulse aligned with the positive *x*-axis. However, invoking this simplification does not eliminate the possibility of alternating-phase RF excitation. Adding π/TR to the "off-resonance" factor $\Delta\omega$ is equivalent to shifting the rotating frame by 180° every repetition, effectively causing pulses along the positive *x*-axis to "alternate" with respect to the common rotating frame. Now, by definition,

$$\mathbf{M}(TR^{+}) = \mathbf{R}(\alpha)\mathbf{M}(TR^{-}), \tag{10}$$

and in the steady state, where $\mathbf{M}(TR^{+}) = \mathbf{M}(0^{+})$, Eq. 10 can be substituted into Eq. 8 (evaluated at $t = TR^{-}$) to provide

$$\begin{aligned} \mathbf{M}(TR^{-}) &= e^{\mathbf{A}\cdot TR}\mathbf{R}(\alpha)\mathbf{M}(TR^{-}) + \left(e^{\mathbf{A}\cdot TR} - \mathbf{I}\right)\mathbf{A}^{-1}\mathbf{C} \\ \left(\mathbf{I} - e^{\mathbf{A}\cdot TR}\mathbf{R}(\alpha)\right)\mathbf{M}(TR^{-}) &= \left(e^{\mathbf{A}\cdot TR} - \mathbf{I}\right)\mathbf{A}^{-1}\mathbf{C} \\ \mathbf{M}_{\mathrm{SS}} &= \left[\mathbf{I} - e^{\mathbf{A}\cdot TR}\mathbf{R}(\alpha)\right]^{-1}\left(e^{\mathbf{A}\cdot TR} - \mathbf{I}\right)\mathbf{A}^{-1}\mathbf{C} \end{aligned} \tag{11}$$

which is the signal equation for two-compartment bSSFP in the following work.

I.3.2 Spoiled Gradient-Recalled Echo (SPGR)

Spoiled gradient echo sequences are among the simplest MRI pulse sequences, and are often used to create T_1- and T_2^{*}-weighted images. Like bSSFP sequences, they use gradients to refocus spins into an echo, but are then subjected to magnetic fields which eliminate all net transverse magnetization prior to the next RF excitation pulse. These "spoilers" can be realized by either a gradient pulse (45-48), a radiofrequency excitation phase increment (49, 50), or a combination of the two which nulls transverse magnetization in the steady state. Regardless of spoiling scheme, an ideal SPGR pulse sequence will remove all dependence of steady-state signal on transverse relaxation rate. (Once again, T_2^{*} decay between the last excitation pulse and the acquisition can be absorbed into an effective value for M_0.) Under these conditions, the 6x6 matrices **M**, **A**, and **C** in Eq. 6 reduce to

$$\mathbf{M}_{\mathrm{SPGR}} = \begin{bmatrix} M_{z,\mathrm{F}} \\ M_{z,\mathrm{S}} \end{bmatrix},$$

$$\mathbf{A}_{\mathrm{SPGR}} = \begin{bmatrix} -R_{1,\mathrm{F}} - k_{\mathrm{FS}} & k_{\mathrm{SF}} \\ k_{\mathrm{FS}} & -R_{1,\mathrm{S}} - k_{\mathrm{SF}} \end{bmatrix},$$

and

$$\mathbf{C}_{\mathrm{SPGR}} = M_0 \begin{bmatrix} R_{1,\mathrm{F}} f_{\mathrm{F}} \\ R_{1,\mathrm{S}} f_{\mathrm{S}} \end{bmatrix}.$$

Furthermore, the refocused gradient-echo signal equation (Eq. 11) can be reduced to

$$\mathbf{M}_{\mathrm{SS}} = M_0 \sin(\alpha)\left[\mathbf{I} - \mathrm{e}^{\mathbf{A}_{\mathrm{SPGR}} \cdot TR} \cos(\alpha)\right]^{-1} \left(\mathbf{I} - \mathrm{e}^{\mathbf{A}_{\mathrm{SPGR}} \cdot TR}\right) \begin{bmatrix} f_{\mathrm{F}} \\ f_{\mathrm{S}} \end{bmatrix}, \quad \textbf{(12)}$$

because

$$\mathbf{C}_{\mathrm{SPGR}} = -M_0 \mathbf{A}_{\mathrm{SPGR}} \begin{bmatrix} f_{\mathrm{F}} \\ f_{\mathrm{S}} \end{bmatrix}, \quad \textbf{(13)}$$

$\mathbf{R}_{\mathrm{SPGR}}(\alpha)$ reduces to the 2x2 identity matrix scaled by $\cos(\alpha)$, and the steady-state longitudinal magnetization is measured via excitation with a final α_x pulse. Although noise in MR magnitude images has been shown to follow the Rice distribution (51), it is assumed by this work that the steady-state signal magnitude $\left|M_{x,\mathrm{F}} + M_{x,\mathrm{S}} + iM_{y,\mathrm{F}} + iM_{y,\mathrm{S}}\right|$ in each sequence is measured with additive Gaussian noise. This approximation is nearly correct as long as the signal remains above approximately twice the noise floor (52), a very loose constraint for quantitative MR using simple gradient-echo sequences.

I.4 The Cramer-Rao Lower Bound

Consider a model $g(\mathbf{x}, \boldsymbol{\theta})$, where $\mathbf{x} \in \mathbb{R}^N$ is an independent parameter vector (e.g., RF pulse flip angles) and $\boldsymbol{\theta} \in \mathbb{R}^M$ is a vector of model parameters (e.g., two-pool parameters in Fig 1). Assume we have a random estimate $\hat{\boldsymbol{\theta}}$ of model parameters based

on noisy observations, $\mathbf{y} \in \mathbb{R}^N$. This estimate of model parameters abides by a probability distribution described by a covariance matrix, $\boldsymbol{\Sigma}_{\hat{\boldsymbol{\theta}}}$, bounded by the Cramer-Rao lower bound (CRLB) (53):

$$\boldsymbol{\Sigma}_{\hat{\boldsymbol{\theta}}} \geq \frac{\partial \mathrm{E}[\hat{\boldsymbol{\theta}}]}{\partial \boldsymbol{\theta}} \boldsymbol{\mathcal{F}}^{-1} \frac{\partial \mathrm{E}[\hat{\boldsymbol{\theta}}]}{\partial \boldsymbol{\theta}}^{T}, \tag{14}$$

where $\boldsymbol{\mathcal{F}}$ is the Fisher information matrix (FIM), $\mathrm{E}[\cdot]$ is the expectation operator, $\boldsymbol{\mathcal{A}} \geq \boldsymbol{\mathcal{B}}$ implies that $(\boldsymbol{\mathcal{A}} - \boldsymbol{\mathcal{B}})$ is a nonnegative-definite matrix, and the derivative of one vector with respect to another follows the convention $(\partial \mathbf{a}/\partial \mathbf{b})_{ij} \equiv \partial a_i / \partial b_j$. The positive square roots of the diagonal elements of this covariance matrix are then lower bounds of the standard deviation of the estimated model parameters

$$\sigma_{\theta_j} \geq \sqrt{\left(\frac{\partial \mathrm{E}[\hat{\boldsymbol{\theta}}]}{\partial \boldsymbol{\theta}} \boldsymbol{\mathcal{F}}^{-1} \frac{\partial \mathrm{E}[\hat{\boldsymbol{\theta}}]}{\partial \boldsymbol{\theta}}^{T} \right)_{jj}}, \tag{15}$$

which can inform on how practically identifiable each model parameter is under specific experimental conditions. It should be noted that maximum likelihood estimators such as minimized sum-squared-error in the presence of normally distributed noise have been proven (54) to achieve the CRLB if such a bound is attainable; however, nonlinearity in the signal within a statistically relevant range of the true intrinsic parameters $\boldsymbol{\theta}$ can increase the actual estimate variance substantially over the CRLB. Nevertheless, in the experimental portion of the following work, the statistic is presented as a definite variance rather than a lower bound.

The central element of Eq. 15, the FIM, is a matrix populated by expected curvature values of the parameter vector $\boldsymbol{\theta}$'s *M*-dimensional log-likelihood hypersurface.

The fact that an estimate's maximal precision is defined by the shape of its probability manifold may be somewhat intuitive: if the estimate's "probability peaks" are sharp, the probability maximum will be better defined and thus less susceptible to noise. Calculation of the FIM is straightforward: when observed data y_i, i = 1 to N, are normally distributed about $g(x_i, \boldsymbol{\theta})$ with variance σ_i^2, the FIM can be calculated as

$$\mathcal{F}_{jk} = \sum_{i=1}^{N} \left(\frac{1}{\sigma_i^2} \frac{\partial g_i}{\partial \theta_j} \frac{\partial g_i}{\partial \theta_k} \right), \tag{16}$$

or, in matrix form as

$$\boldsymbol{\mathcal{F}} = \mathbf{J}^T \boldsymbol{\Sigma}^{-1} \mathbf{J} \tag{17}$$

where $\mathbf{J}_{ij} = \partial g_i / \partial \theta_j$ (the Jacobian matrix) and $\boldsymbol{\Sigma}$ is the diagonal covariance matrix of the added noise.

The CRLB also includes the estimator gradient matrix $\partial \mathrm{E}[\hat{\boldsymbol{\theta}}] / \partial \boldsymbol{\theta}$, which incorporates the gradient of the estimator bias. For unbiased estimators, $\mathrm{E}[\hat{\boldsymbol{\theta}}] = \boldsymbol{\theta}$, so $\partial \mathrm{E}[\hat{\boldsymbol{\theta}}] / \partial \boldsymbol{\theta} = \mathbf{I}$, the identity matrix, and does not contribute to the CRLB. For biased estimators, however, this term does not reduce to identity and can be computed numerically by repeated parameter estimation with varied model parameter values. An informal derivation of the CRLB follows.

I.4.1 Informal Derivation of the Cramer-Rao Bound

The score vector **v** of an estimate, which is the relative rate of change of the signal likelihood function f with respect to model parameters, is defined as

$$v_j \equiv \frac{1}{f(\mathbf{y}, \boldsymbol{\theta})} \frac{\partial f(\mathbf{y}, \boldsymbol{\theta})}{\partial \theta_j} = \frac{\partial}{\partial \theta_j} \log f(\mathbf{y}, \boldsymbol{\theta}). \tag{18}$$

When *f* is multivariate Gaussian, **v** can be reduced to

$$v_j = \sum_{i=1}^{N} \frac{\left(\mathrm{y}_i - \mathrm{g}_i(\boldsymbol{\theta})\right)}{\sigma_i^2} \frac{\partial \mathrm{g}_i(\boldsymbol{\theta})}{\partial \theta_j}, \tag{19}$$

or, in matrix form as a column vector,

$$\mathbf{v} = \mathbf{J}^T \boldsymbol{\Sigma}^{-1} \mathbf{r}, \tag{20}$$

where **J** is the Jacobian matrix as traditionally defined for the true signal $\mathbf{g}(\boldsymbol{\theta})$, $\boldsymbol{\Sigma}$ is the diagonal covariance matrix of the added noise, and **r** is a column vector of noise values. Note that since the expectation of additive noise is zero, the expectation of the score vector is a zero vector. The covariance matrix of the score vector **v**, also known as Fisher information, is then calculated as follows:

$$\begin{aligned} \mathrm{cov}(\mathbf{v}) &= \mathrm{E}\left[\mathbf{v}\mathbf{v}^T\right] - \mathrm{E}[\mathbf{v}]\mathrm{E}\left[\mathbf{v}^T\right] = \mathrm{E}\left[\mathbf{J}^T\boldsymbol{\Sigma}^{-1}\mathbf{r}\mathbf{r}^T\boldsymbol{\Sigma}^{-1}\mathbf{J}\right] - \mathbf{0} \\ &= \mathbf{J}^T\boldsymbol{\Sigma}^{-1}\mathrm{E}\left[\mathbf{r}\mathbf{r}^T\right]\boldsymbol{\Sigma}^{-1}\mathbf{J} = \mathbf{J}^T\boldsymbol{\Sigma}^{-1}\boldsymbol{\Sigma}\boldsymbol{\Sigma}^{-1}\mathbf{J} \\ &= \mathbf{J}^T\boldsymbol{\Sigma}^{-1}\mathbf{J}, \end{aligned} \tag{21}$$

where the symbol $\mathrm{E}[\cdot]$ represents the expectation operation over the likelihood function *f* with respect to **y**. Furthermore, the covariance of **v** with the estimate vector $\hat{\boldsymbol{\theta}}$ can be calculated as:

$$\begin{aligned} \mathrm{cov}\left(\hat{\boldsymbol{\theta}}, \mathbf{v}\right) &= \mathrm{E}\left[\hat{\boldsymbol{\theta}}, \mathbf{v}^T\right] - \mathrm{E}\left[\hat{\boldsymbol{\theta}}\right]\mathrm{E}\left[\mathbf{v}^T\right] = \mathrm{E}\left[\hat{\boldsymbol{\theta}}\left(\frac{1}{f(\mathbf{y},\boldsymbol{\theta})}\frac{\partial}{\partial\boldsymbol{\theta}} f(\mathbf{y},\boldsymbol{\theta})\right)\right] \\ &= \int \hat{\boldsymbol{\theta}}\left(\frac{\partial}{\partial\boldsymbol{\theta}} f(\mathbf{y},\boldsymbol{\theta})\right)\mathrm{d}\mathbf{y}. \end{aligned} \tag{22}$$

Because the estimate $\hat{\boldsymbol{\theta}}$ is not directly dependent on underlying parameters $\boldsymbol{\theta}$, the order of differentiation and integration can be reversed, leaving

$$\mathrm{cov}\left(\hat{\boldsymbol{\theta}}, \mathbf{v}\right) = \frac{\partial}{\partial\boldsymbol{\theta}} \int \hat{\boldsymbol{\theta}}\, f(\mathbf{y},\boldsymbol{\theta})\, \mathrm{d}\mathbf{y} = \frac{\partial \mathrm{E}[\hat{\boldsymbol{\theta}}]}{\partial\boldsymbol{\theta}}. \tag{23}$$

Substituting Eq. 23 into the multivariate Cauchy-Schwarz inequality results in a formal statement of the Cramer-Rao bound:

$$\begin{aligned} \operatorname{cov}\left(\hat{\boldsymbol{\theta}}\right) &\geq \operatorname{cov}\left(\hat{\boldsymbol{\theta}}, \mathbf{v}\right) \operatorname{cov}\left(\mathbf{v}\right)^{-1} \operatorname{cov}\left(\hat{\boldsymbol{\theta}}, \mathbf{v}\right)^{T} \\ &\geq \frac{\partial \mathrm{E}[\hat{\boldsymbol{\theta}}]}{\partial \boldsymbol{\theta}} \left[\mathbf{J}^{T} \boldsymbol{\Sigma}^{-1} \mathbf{J} \right]^{-1} \frac{\partial \mathrm{E}[\hat{\boldsymbol{\theta}}]}{\partial \boldsymbol{\theta}}^{T} . \end{aligned} \tag{24}$$

Note that Eq. 24 states that the distribution of an estimate is inversely proportional to the model's squared sensitivity to the estimated parameter, which is a generalization of the well-known propagation of error theorem to a possibly biased set of estimates given multiple random points of data. In a further, potentially more significant parallel to the propagation of error theorem, the uncertainty in parameter estimates defined by the CRLB scales inversely with SNR.

I.4.2 Decreasing Variance by Constraining Parameters

Due to the fact that the FIM is purely a function of the true signal and noise variance, information content is unaffected by the choice of estimator. Thus, information is conserved even when the contrast of the estimate is enhanced; the multiplication by $\partial \mathrm{E}[\hat{\boldsymbol{\theta}}] / \partial \boldsymbol{\theta}$ causes biased estimates which enjoy greater contrast than their unbiased counterparts to receive a proportional penalty to random deviation. Only by constraining covarying parameters to *a priori* values and eliminating their respective elements from the FIM before inverting—or by decreasing the problem dimensionality in any similar manner—can estimate precision truly be improved. However, this improvement comes at the cost of accuracy: bias is introduced into estimates when model parameters are constrained to guesses.

Stated mathematically, the conditional covariance matrix of the parameters remaining unconstrained is the Schur complement of the covariance matrix block pertaining to the constrained parameters (55):

$$\operatorname{cov}\left(\hat{\boldsymbol{\theta}}_{\text{free}}\right) \geq \frac{\partial \mathrm{E}[\hat{\boldsymbol{\theta}}_{\text{free}}]}{\partial \boldsymbol{\theta}_{\text{free}}}\left[\boldsymbol{\Sigma}_{\text{free}} - \boldsymbol{\Sigma}_{\text{f,c}}\left(\boldsymbol{\Sigma}_{\text{cons}}^{-1}\right)\boldsymbol{\Sigma}_{\text{c,f}}\right]\frac{\partial \mathrm{E}[\hat{\boldsymbol{\theta}}_{\text{free}}]}{\partial \boldsymbol{\theta}_{\text{free}}}^{T}, \quad \textbf{(25)}$$

where $\operatorname{cov}\left(\hat{\boldsymbol{\theta}}\right) \geq \left[\mathbf{J}^{T}\boldsymbol{\Sigma}^{-1}\mathbf{J}\right]^{-1} = \begin{bmatrix} \boldsymbol{\Sigma}_{\text{cons}} & \boldsymbol{\Sigma}_{\text{c,f}} \\ \boldsymbol{\Sigma}_{\text{f,c}} & \boldsymbol{\Sigma}_{\text{free}} \end{bmatrix}$ and $\hat{\boldsymbol{\theta}} = \begin{bmatrix} \hat{\boldsymbol{\theta}}_{\text{cons}} \\ \hat{\boldsymbol{\theta}}_{\text{free}} \end{bmatrix}$, and the subscripts "free" and "cons" refer to the freely fitted and constrained parameters. Readers should note that Eq. 25 implies the reduction in parametric uncertainty due to constraint is proportional to the free parameters' squared covariance with constrained parameters ($\boldsymbol{\Sigma}_{\text{f,c}}$).

CHAPTER II

EXPERIMENTAL METHODS

II.1 Unconstrained mcDESPOT Cramer-Rao Bounds

For various model tissues (Table 1, parameter sets 1-5) the CRLB of fitted parameters were calculated using Eq. 15 and for two previously published mcDESPOT methods. The first mcDESPOT method (12) was comprised of 7 SPGR acquisitions with varied RF flip angle (α_{SPGR} = 2°, 4°, … , 14°; TR_{SPGR} = 6.5 ms; BW_{SPGR} = 20 kHz) and 9 bSSFP acquisitions with varied RF flip angle (α_{SSFP} = 6°, 14°, … , 70°; TR_{SSFP} = 5 ms; BW_{SSFP} = 60 kHz). The second, more recently reported mcDESPOT method (38), included the same SPGR acquisitions but 18 SSFP acquisitions using the same 9 flip angles each repeated with and without a 180° RF phase increment per TR period

Table 1. **Tissue parameter sets.** Set 5 represents a scenario in which the T_1/T_2 ratios of each compartment are equal. Sets 6-8 were used with a range of f_F values and varying one other parameter within the range provided. Sets 9-11 demonstrate by example different tissue models that result in effectively identical mcDESPOT signals.

Parameter Set	$T_{1,S}$ (ms)	$T_{1,F}$ (ms)	$T_{2,S}$ (ms)	$T_{2,F}$ (ms)	f_F (%)	τ_F (ms)
1	800	450	100	20	20	100
2	800	450	100	20	20	400
3	1500	450	100	20	20	100
4	1500	450	100	20	20	400
5	2250	450	100	20	20	100
6	800	450	75 - 150	20	5-45	100
7	800	450	100	15 - 30	5-45	100
8	800	450	100	20	5-45	20 - $\gg T_2$
9	970	415	80.0	12	15	90
10	965	527	83.7	16.6	23	150
11	965	579	86.9	19.3	28	200

($\Delta ø$ = 180° or 0°). This second method allows fitting of an off-resonance term, $\Delta\omega$, as an 8th independent model parameter, although the present work used the on-resonance condition for all cases. In order to compare these two methods assuming equal total acquisition time, the original method was calculated using 18 SSFP acquisitions by simply repeating each SSFP measurement one time.

As noted above, the estimator gradient matrix terms in Eq. 15 were ignored for the unconstrained fitting analysis. The FIM was computed using Eq. 17, which includes the Jacobian and noise covariance matrices. The Jacobian matrix was calculated as defined above, $\mathbf{J}_{ij} = \partial g_i / \partial \theta_j$, where the derivative of the signal equation, Eq. 12 for SPGR and Eq. 11 for SSFP, was evaluated at the 25 different RF flip angles (x_i; 7 for SPGR and 18 for SSFP) and with respect to 7 (or 8) different model parameters (θ_j). Each derivative was estimated from a forward-difference calculation of the signal with respect to a step size in the model parameter by a factor of 1×10^{-4}. The noise covariance matrix was computed assuming Gaussian noise with standard deviations $\sigma_{\mathrm{SPGR}} = 1 \times 10^{-3}$ (a.u.) and $\sigma_{\mathrm{SSFP}} = \sqrt{3}\sigma_{\mathrm{SPGR}}$ due to the greater receiver BW for the SSFP acquisitions. The noise was defined as uncorrelated between acquisitions, so the covariance matrix was diagonal. At these values of noise variance, the maximum image signal-to-noise ratio (SNR), defined as the maximum image intensity divided by the standard deviation of the added noise, was approximately 100 for all tissue models.

As an informative measure, the condition number of each Jacobian matrix was calculated as the ratio of its highest singular value to its lowest. This value was a rough estimate of the ratio of relative error in estimated parameters to the relative error in signal (56). Specifically, an infinite condition number corresponds to a rank-deficient Jacobian

and unsolvable estimation problem, while a large condition number can indicate that certain parameters may be unidentifiable at feasible SNRs.

II.2 Constrained mcDESPOT Cramer-Rao Bounds

The CRLB of fitted parameters were also calculated while constraining both transverse relaxation rates ($R_{2,S}$, $R_{2,F}$) and the water exchange rate (k_{FS}). For the best case scenario, when $R_{2,S}$, $R_{2,F}$ and k_{FS} were constrained to their correct model values, the estimator gradient matrix remained an identity matrix, and the Jacobian was reduced by removing the columns associated with the three constrained parameters. Fisher information matrices and CRLB were then calculated as usual using Eq. 17 and 15 and assuming parameter set 1 in Table 1. For the more general, biased, scenario, when *a priori* constraints were not correct, the estimator gradient matrix was determined numerically as follows. Noiseless mcDESPOT signals were generated using various tissue models (Table 1, parameter sets 6-8) and these signals were fitted with the signal equations (Eq. 12 and 11) using a minimum χ^2 criteria (57) and while constraining $R_{2,S}$, $R_{2,F}$ and k_{FS} to one of three sets of values (A-C, Table 2). Each fit was repeated with

Table 2. Time constant constraints

Parameter Set	$T_{2,S}$ (ms)	$T_{2,F}$ (ms)	τ_F (ms)
A	150	20	100
B	100	30	100
C	100	20	67
D	125	35	200

varied initial conditions in order to ensure that the global minimum χ^2 value was found, which thus provided the expected value of fitted parameters, $E[\hat{\theta}]$. This process was repeated while individually perturbing each model parameter by a factor 1×10^{-4} and then the estimator gradient matrix, $\partial E[\hat{\theta}]/\partial\theta$, was formed from the series of forward-difference derivative approximations. The noise covariance matrix was generated as above and, finally, the CRLB was calculated using Eq. 15.

II.3 Validation of the Cramer-Rao Bound

Monte Carlo simulations were used to validate both the unbiased and biased CRLB calculations using model tissue 1 (Table 1) and constraint set D (Table 2). Equations 11 and 12 were used to generate mock mcDESPOT data to which random Gaussian noise was added. For the unconstrained case, with 7 or 8 free model parameters and relatively large CRLB, a very high SNR was used to allow robust and efficient fitting; $\sigma_{\mathrm{SPGR}} = 1 \times 10^{-7}$ (a.u.) and $\sigma_{SSFP} = \sqrt{3}\sigma_{SPGR}$. Due to the constrained scenario's lower CRLB, a correspondingly smaller SNR was used to ensure that variance in parameter estimates was dominated by propagated noise and not inaccuracies in the fitting algorithm; $\sigma_{\mathrm{SPGR}} = 1 \times 10^{-3}$ (a.u.) and $\sigma_{SSFP} = \sqrt{3}\sigma_{SPGR}$. For both cases then, the noisy data were fitted with Eq. 11 and 12 to a minimum χ^2 criterion using standard non-linear regression tools (*lsqnonlin* function in MATLAB) and varied initial conditions. Each signal was fitted 100 times using initial guesses that were randomly distributed about the known solution with standard deviation equal to 10 times the predicted CRLB. If the best 20 of these 100 fits converged to solutions with <0.01% parameter variability, then the solution was considered the global minimum. This threshold was chosen to be

significantly less than the variability in parameter solutions predicted by the CRLB. If this stop criterion was not achieved, the algorithm was repeated with 100 new seed vectors. After satisfactorily fitting 10000 signals with independently generated additive noise, the variances of all fitted parameters were calculated and compared to the CRLB.

CHAPTER III

RESULTS

The Monte Carlo simulations provided parameter variances that agreed well with the calculated Cramer-Rao lower bounds. The panels in Fig 2 consist of histograms displaying the results of both unbiased and biased fast-signal fraction estimates from the Monte Carlo simulations, while the superimposed curves represent predicted distributions based on the calculated CRLB. Similar results were found for all model parameters—CRLB and Monte Carlo derived variances differed by no more than 8% for any parameter.

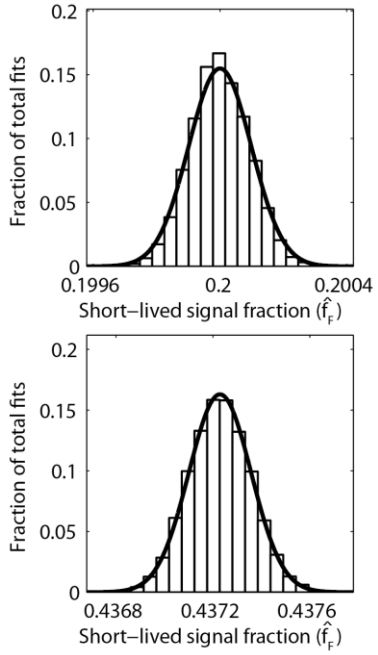

Figure 2. Monte Carlo simulation results and their theoretical Cramer-Rao bounds. The histograms represent bins created from 10,000 trials, while the overlaid curves follow a Gaussian distribution with mean f_F and variance equal to the CRLB. Top: unbiased 7-parameter fitting using parameter set 1 in Table 1 at SNR~10^6; bottom: biased 4-parameter fitting using intrinsic parameters from set 1 in Table 1 and constraints from set D in Table 2 at SNR~10^2.

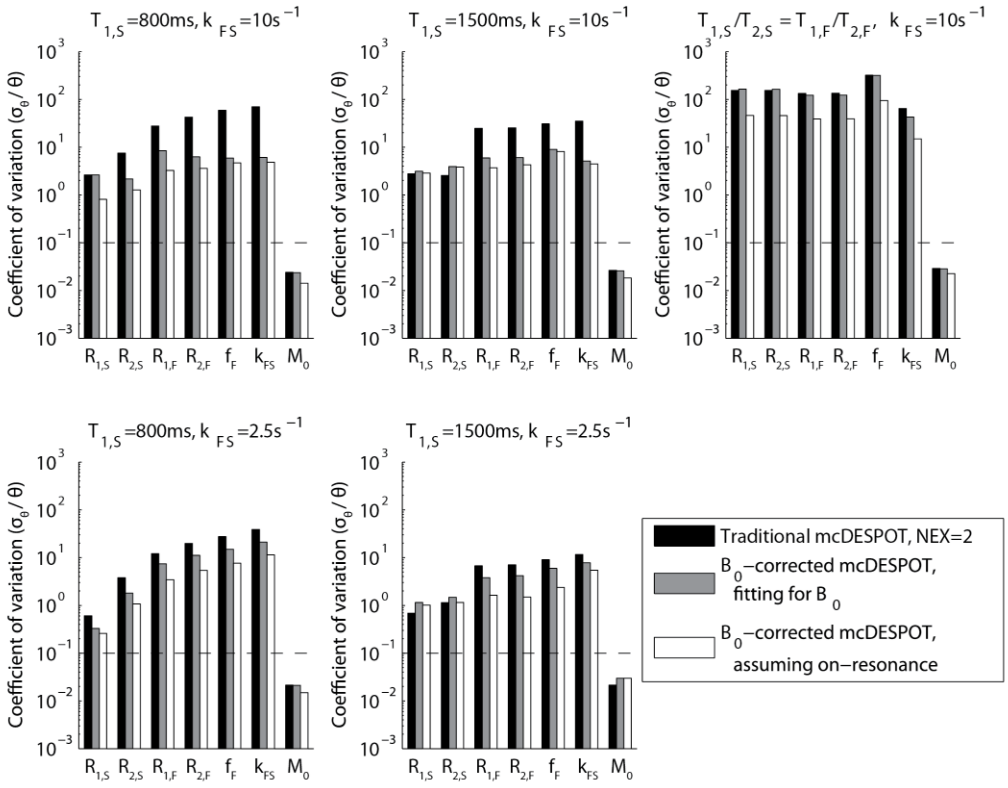

Figure 3. Unconstrained Cramer-Rao bounds as coefficients of variation. Three methods are presented using five sets of intrinsic parameter values (1-5 in Table 1). This study was performed at $\sigma_{SPGR} = 1 \times 10^{-3}$ (a.u.), which corresponds to a clinically-feasible SNR for gradient echo sequences, and it should be noted that coefficients of variation scale with image SNR. The dotted lines on each plot are a reference goal ($c_\theta \leq 10\%$) for quantitative precision.

When examining unconstrained estimators of all model parameters, the Cramer-Rao bounds were very high at feasible signal-to-noise ratios. Figure 3 shows the results of the unbiased CRLB calculations presented as coefficients of variation ($c_\theta = \sigma_\theta / \theta$) at $\sigma_{SPGR} = 1 \times 10^{-3}$ (a.u.). The CRLB vary significantly between model tissues, but in all cases $c_\theta >> 10\%$ for all parameters except total proton density, M_0. (In many cases, a practical goal for estimate precision is $c_\theta \leq 10\%$.) These large CRLB for mcDESPOT

agree with the condition number ~10^5 found for the model's Jacobian matrix for a variety of typical tissue parameters, indicating a very large propagation of error from image signal intensities to estimated model parameters. Interestingly, evaluating the forward model using both alternating and non-alternating RF phase cycling schemes improved estimate precision by up to an order of magnitude. While this was not a sufficient improvement to guarantee identifiable estimates at practical SNR, it is worth noting that even with the addition of an 8th free parameter, $\Delta\omega$, the precision of other parameter estimates improved. Neglecting this parameter while still acquiring at both phase cycling

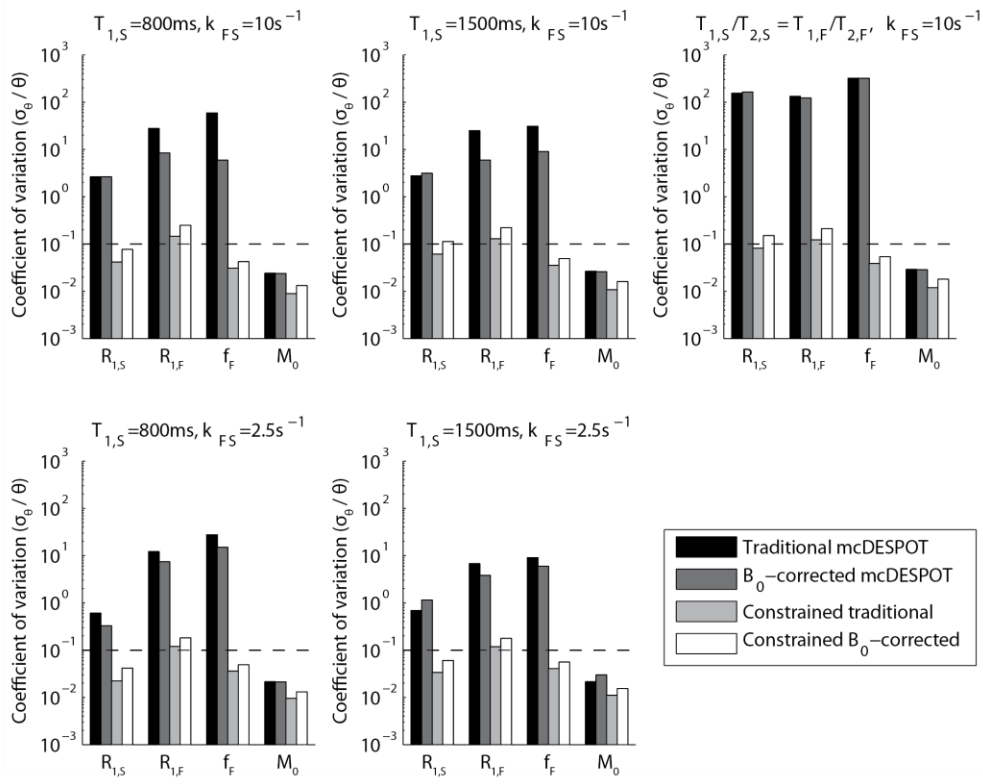

Figure 4. Constrained Cramer-Rao bounds as coefficients of variation. Parameter values are listed as sets 1-5 in Table 1, and accurate constraints are assumed. This study was performed at σ_{SPGR} = 1 x 10^{-3} (a.u.), which corresponds to a clinically-feasible SNR for gradient echo sequences, and it should be noted that coefficients of variation scale with image SNR. The dotted lines on each plot are a reference goal ($c_\theta \leq 10\%$) for quantitative precision.

schemes gives an additional, sometimes significant improvement to estimate precision, but forfeits the inhomogeneity-correcting accuracy gains detailed by Deoni (38).

The scenario in which exchange and transverse relaxation rates are constrained provided much improved precision; Fig 4 shows an improvement in up to three orders of magnitude, regardless of bSSFP acquisition scheme. Again, this coincides well with an

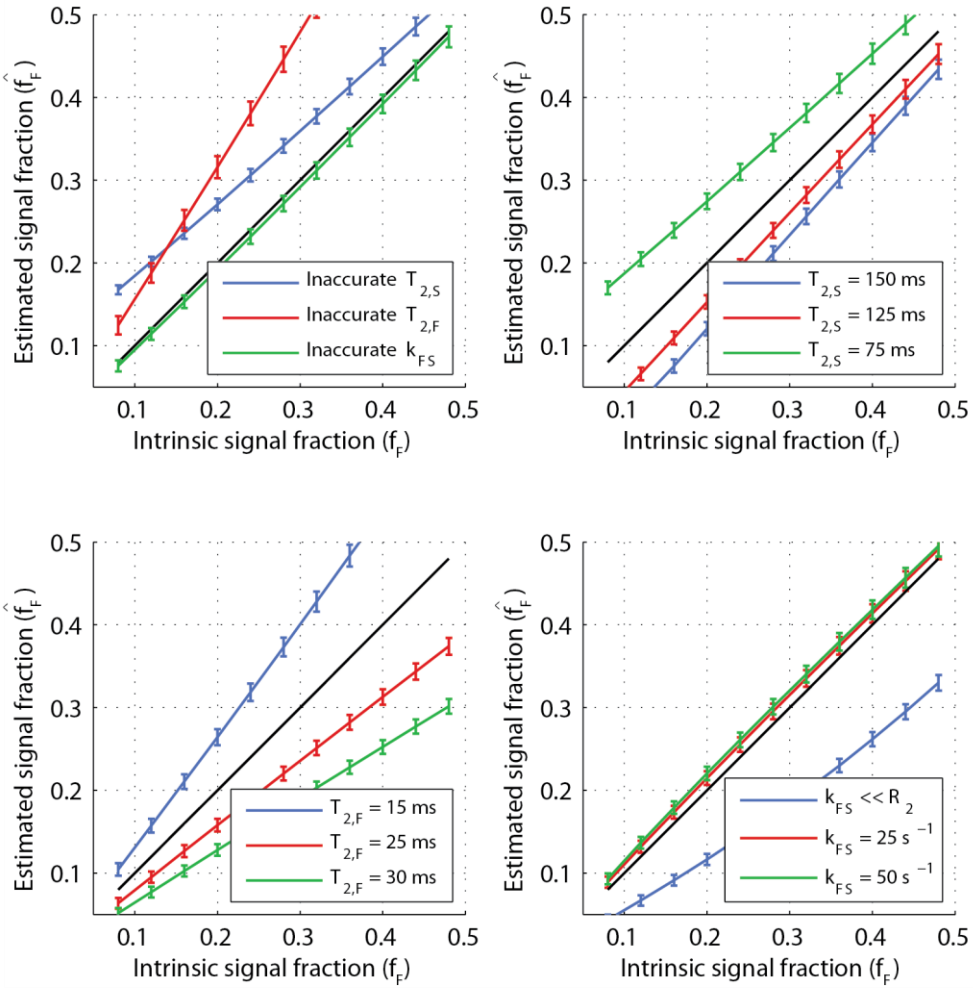

Figure 5. Biased estimates of fast-decaying signal fraction and their uncertainties. Top-left: fitting a signal created by parameters in set 1 from Table 1 using the constraint sets A-C in Table 2; top-right: fitting a signal created by parameters in the range of set 6 from Table 1 using the constraint set A in Table 2; bottom-left: parameter set 7 and constraint set A; bottom-right: parameter set 8 and constraint set A. In all scenarios, CRLB are calculated using $\sigma_{SPGR} = 1 \times 10^{-3}$ (a.u.).

observed reduction in the condition number of the Jacobian to ~100 when columns with the signal derivative with respect to $R_{2,S}$, $R_{2,F}$ and k_{FS} were removed. The price paid for the improved estimate precision is an increased estimate bias. Figure 5 demonstrates the relationship between short-lived signal fraction estimates ($\hat{f}_F$) and corresponding true model values (f_F) for two different tissue models and a variety of *a priori* $R_{2,S}$, $R_{2,F}$ and k_{FS} constraints. The error bars represent estimate standard deviations based on the CRLB at $\sigma_{SPGR} = 1 \times 10^{-3}$ (a.u.). In general, although the estimates showed a substantial bias (more than 100% of the intrinsic value in some cases), there is a monotonic, nearly linear relationship between the estimates and the true model values.

CHAPTER IV

DISCUSSION & CONCLUSIONS

Numerical computations demonstrate that mcDESPOT, as previously described, cannot provide parameter estimates of a two-pool system with usable precision. A less rigorous but perhaps more intuitive demonstration of this can be seen in Fig 6, which shows mcDESPOT signals from 3 different model tissues (Table 1, parameter sets 9-11) and the differences between these signals compared with added noise at the $\sigma_{SPGR} = 1 \times 10^{-3}$ (a.u.) level. In this example, f_F varied between 15% and 28% across the three tissues,

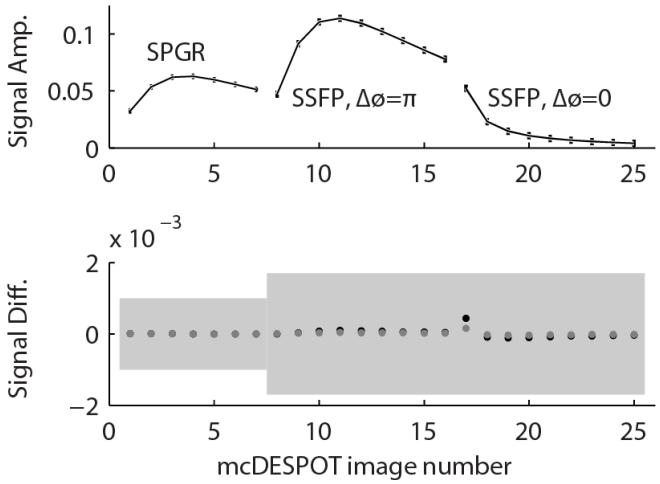

Figure 6. mcDESPOT signal differences relative to appropriate noise levels. Top: a reference mcDESPOT signal containing two bSSFP curves (using both alternating and non-alternating RF excitation phase every repetition) and one SPGR curve. Bottom: differences between the reference signal above and signals with very distinct parameter values. For example, f_F values vary between 15% and 28%. Nevertheless, the uncertainty due to noise is still very large compared to the hardly distinguishable signal differences, so one would expect difficulty in differentiating the signals.

but their resulting mcDESPOT signal differences are approximately 3 orders of magnitude smaller than the standard deviation of the added noise. Clearly, with this level of noise, any of these three signals could be equally-well fitted with any of the three parameters sets.

These findings of impractically high parameter variance from mcDESPOT, however, are incongruent with previous *in vivo* studies, which show maps of mcDESPOT-derived MWF (i.e., f_F in a white matter model) that exhibit relatively low variance (36, 37). It thus appears that the model presented here does not accurately reflect the *in vivo* scenario. Two possible sources for this difference are: 1) the estimator used for the *in vivo* studies, and/or 2) the model used to characterize the tissue. In the first case, it is possible that the solution vectors, $\hat{\theta}$, found in the *in vivo* studies were not at the global χ^2 minimum. This would not be surprising given the large dimensionality (7 or 8 free parameters) of the problem and typically modest SNR expected *in vivo*. In this case, the estimator gradient matrix would not be an identity matrix and its norm would be less than one, resulting in a decrease in the CRLB in accordance with Eq. 15. Figure 7 demonstrates the effects of the mcDESPOT model's local minima on classical optimization methods. When each initial seed parameter is varied by 50% of the true value, classical least-squares optimizations of signal fraction trend toward certain likelihood "trenches", such as a one-pool approximation. In order to address this difficulty, Deoni, et al proposed sophisticated algorithms (12, 38) to solve the least-squares problem, which in-turn may have inadvertently imparted constraints on the solutions.

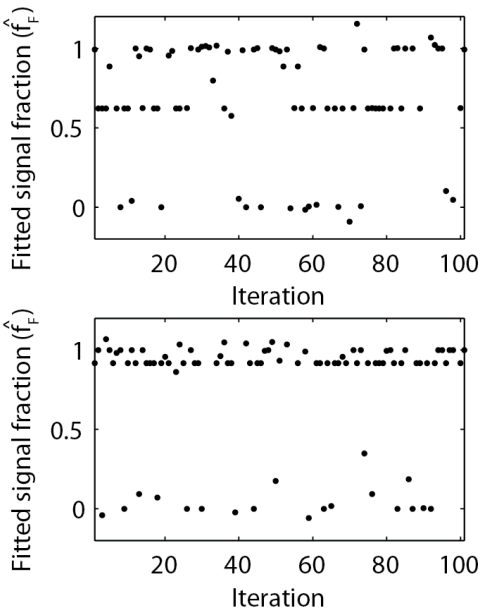

Figure 7. Effect of mcDESPOT dimensionality on fitting difficulty. Each panel represents a different set of additive noise, while each point represents a different optimization seed vector. Note that certain local minima are stable across various noise values (such as those near $f_F = 0$ or 1) while others are sensitive to the noise (such as those near 0.9 or 0.6).

The second case is that the two-pool model, upon which mcDESPOT and the CRLB calculation herein are based, does not satisfactorily describe white matter *in vivo*. In this case, the sensitivity *in vivo* of the signal to an apparent signal fraction or T_2 value may be greater than the sensitivity would be for a perfect two-pool system. For example, magnetization transfer effects, which are not presently incorporated into the mcDESPOT model, are known to affect both bSSFP (58, 59) and SPGR (60) signals. The relatively large macromolecular pool that is thought to exchange magnetization with myelin water (61) will reduce the apparent T_2s in a DESPOT2 (bSSFP) measurement (62) and may result in significantly reduced variance in the estimates of the apparent fast-relaxing signal in a two-pool model. This effect would suggest that the mcDESPOT measure of

MWF is to some degree a measure of macromolecular proton fraction, much like a qMT measurement provides. Such a scenario would explain the observed correspondence between mcDESPOT measures of MWF and tissue myelination and the apparently high measures of MWF found in gray matter using mcDESPOT (36). At this point, neither the estimator nor the model (nor some combination) can be definitively identified as the source of differences between *in vivo* studies and the CRLB.

Beyond the unconstrained mcDESPOT methods used to date, the results here show that constraining some model parameters—for example, both T_2s and the intercompartmental exchange rate—to *a priori* values allows for much improved precision of the remaining parameter estimates. This particular constraint scenario is presented as an example and is not necessarily the best strategy. Although not shown, a variety of other strategies were investigated and it is worth noting that no combination of constraints was found that provided simultaneous low variance estimates of both k_{FS} and f_F. Thus, in the context of white matter imaging, we conclude that there is no viable mcDESPOT strategy to estimate MWF independently from the effects of inter-compartmental water exchange, or vice versa. Of course, the same is true for a conventional multiple spin echo measurement of transverse relaxation.

In terms of the practicality of estimating an apparent MWF using the constrained mcDESPOT approach evaluated here, accuracy will depend on how well the constrained parameter values can be chosen. The top-left panel in Fig 5 indicates that, when comparing otherwise similar tissues, this constrained mcDESPOT will report on changes or differences in MWF accurately, despite erroneous *a priori* constraints. More specifically, these results suggest that constrained mcDESPOT, measured with peak

image SNR ≈ 100, can identify a difference of as little as 5% intrinsic signal fraction within 95% confidence. Conversely, the other panels of Fig 5 show how differences in water exchange rate and R_2 values will alter the apparent MWF. It may be reasonable to expect $R_{2,F}$ to be relatively invariant across tissues and subjects, at least in the absence of a condition of myelin edema; however, there is good reason to believe that water exchange rates, k_{FS}, will depend on myelin thickness and axon diameter (13, 14), and the intra-/extra-axonal water relaxation rate, $R_{2,S}$, is likely to vary greatly with inflammation. Thus, the utility of constrained mcDESPOT will depend very much on the application, and any interpretation of changes or differences in measured MWFs should consider the potential co-factors.

The observation that the parameter estimate precision can be improved substantially by repeating the bSSFP scan with and without 180° RF phase alteration (although the improvement did not occur under the constrained mcDESPOT scenario) reveals a novel mechanism for further optimizing mcDESPOT or other quantitative studies using bSSFP. Investigation of the parameter covariance matrix (Eq. 14) shows that 180° changes in the RF phase increment alter the sign of some parameter covariances (off-diagonal terms in $\mathbf{\Sigma}_{\hat{\theta}}$), which results in a net reduction in covariance between parameters when signals acquired with both 0° and 180° increments are fitted concurrently. It is conceivable that other RF phase increments offer the effect of further diagonalizing $\mathbf{\Sigma}_{\hat{\theta}}$ and, in turn, improving parameter estimate precision.

In summary, the work detailed here has demonstrated—via analytical statistics validated by Monte Carlo simulation and condition number analysis—the inability of mcDESPOT signals to precisely estimate parameters of a two-pool model with exchange.

Previous demonstrations of low variance parameter estimates from in vivo studies of white matter may be due to the effective constraints being imparted on the parameter estimates in standard mcDESPOT analysis, or may be due to an insufficiency of the two-pool model to describe white matter for these measurements. Regardless of the source of discrepancy, further study is required before mcDESPOT data can be unambiguously interpreted.

REFERENCES

1) Sherwood, L. Human Physiology: from Cells to Systems. Cengage Learning; 2006, p 100.

2) Hakak Y, Walker JR, Li C, Wong WH, Davis KL, et al. Genome-wide expression analysis reveals dysregulation of myelination-related genes in chronic schizophrenia. Proc Nat Acad Sci 2001; 98(8):4746-4751.

3) Davis KL, Stewart DG, Friedman JI, Buchsbaum M, Harvey PD, et al. White matter changes in schizophrenia. Arch Gen Psychiatry. 2003;60(5):443-456.

4) Poon C, Henkelman R. Practical T2 Quantitation for Clinical Applications. Jmri-J Magn Reson Im 1992;2(5):541–553.

5) Prasloski T, Mädler B, Xiang Q-S, MacKay A, Jones C. Applications of Stimulated Echo Correction to Multicomponent T2 Analysis. Magn Reson Med. *In press.*

6) Does M, Snyder R. Multiecho imaging with suboptimal spoiler gradients. J Magn Reson 1998;131(1):25–31.

7) Does M, Gore J. Rapid acquisition transverse relaxometric imaging. J Magn Reson 2000;147(1):116–120.

8) Skinner MG, Kolind SH, Mackay AL. The effect of varying echo spacing within a multiecho acquisition: better characterization of long T2 components. Magn Reson Imaging 2007;25(6):840–847.

9) Dula AN, Gochberg DF, Does MD. Optimal echo spacing for multi-echo imaging measurements of Bi-exponential T2 relaxation. J Magn Reson 2009;196(2):149–156.

10) Oh J, Han ET, Pelletier D, Nelson SJ. Measurement of in vivo multi-component T2 relaxation times for brain tissue using multi-slice T2 prep at 1.5 and 3 T. Magn Reson Imaging 2006;24(1):33–43.

11) Mädler B, AL M. In-vivo 3D Multi-component T2-Relaxation Measurements for Quantitative Myelin Water Imaging at 3T. Proceedings of the 11th scientific meeting, International Society for Magnetic Resonance in Medicine. Seattle, 2006, p 2112.

12) Deoni SCL, Rutt BK, Arun T, Pierpaoli C, Jones DK. Gleaning multicomponent T1 and T2 information from steady-state imaging data. Magn Reson Med 2008;60(6):1372–1387.

13) Dula AN, Gochberg DF, Valentine HL, Valentine WM, Does MD. Multiexponential T2, magnetization transfer, and quantitative histology in white matter tracts of rat spinal cord. Magn Reson Med 2010;63(4):902–909.

14) Harkins KD, Dula AN, Does MD. Effect of intercompartmental water exchange on the apparent myelin water fraction in multiexponential T(2) measurements of rat spinal cord. Magn Reson Med 2011 *epub ahead of print*, Jun 28 2011.

15) McDonald WI, Compston A, Edan G, Goodkin D, Hartung HP, et al. Recommended diagnostic criteria for multiple sclerosis: guidelines from the international panel on the diagnosis of multiple sclerosis. Annals of Neurology 2001; 50(1):121-127.

16) Polman CH, Reingold SC, Edan G, Filippi M, Hartung HP, et al. Diagnostic criteria for multiple sclerosis: 2005 revisions to the "McDonald Criteria". Annals of Neurology 2005; 58(6):840-846.

17) Polman CH, Reingold SC, Banwell B, Clanet M, Cohen JA, et al. Diagnostic criteria for multiple sclerosis: 2010 revisions to the McDonald Criteria. Annals of Neurology 2011; 69(2):292-302.

18) Thorpe JW, Kidd D, Kendall BE, Tofts PS, Barker GJ, et al. Spinal cord MRI using multi-array coils and fast spin echo. I. Technical aspects and findings in healthy adults. Neurology 1993; 43(12):2625-2631.

19) Thorpe JW, Halpin SF, MacManus DG, Barker GJ, Kendall BE, Miller DH. A comparison between fast and conventional spin-echo in the detection of multiple sclerosis lesions. Neuroradiology 1994; 36(5):388-392.

20) Vasilescu V, Katona E, Simplaceanu V, Demco D. Water compartments in the myelinated nerve. III. Pulsed NMR results. Experientia 1978; 34(11):1443–1444.

21) Menon R, Rusinko M, Allen P. Proton Relaxation Studies of Water Compartmentalization in a Model Neurological System. Magn Reson Med 1992;28(2):264–274.

22) MacKay A, Whittall K, Adler J, Li D, Paty D, Graeb D. In-Vivo Visualization of Myelin Water in Brain by Magnetic-Resonance. Magn Reson Med 1994;31(6):673–677.

23) Does M, Snyder R. Multiexponential T-2 relaxation in degenerating peripheral nerve. Magn Reson Med 1996;35(2):207–213.

24) Whittall KP, MacKay AL. Quantitative Interpretation of NMR Relaxation Data. J Magn Reson 1989;84:134–152.

25) Whittall K, MacKay A, Graeb D, Nugent R, Li D, Paty D. In vivo measurement of T-2 distributions and water contents in normal human brain. Magn Reson Med 1997;37(1):34–43.

26) Schmierer K, Tozer DJ, Scaravilli F, Altmann DR, Barker GJ, et al. Quantitative magnetization transfer imaging in postmortem multiple sclerosis brain. J Magn Reson Im 2007; 26(1):41-51.

27) Ou X, Sun SW, Liang HF, Song SK, Gochberg DF. Quantitative magnetization transfer measured pool-size ratio reflects optic nerve myelin content in ex vivo mice. Magn Reson Med 2009; 61(2):364-371.

28) Levesque IR, Giacomini PS, Narayanan S, Ribeiro LT, Sled JG, et al. Quantitative magnetization transfer and myelin water imaging of the evolution of acute multiple sclerosis lesions. Magn Reson Med 2010; 63(3):633-640.

29) Henkelman RM, Huang X, Xiang QS, Stanisz GJ, Swanson SD, Bronskill MJ. Quantitative interpretation of magnetization transfer. Magn Reson Med 1993; 29(6):759-766.

30) Gochberg DF, Kennan RP, Gore JC. Quantitative studies of magnetization transfer by selective excitation and T1 recovery. Magn Reson Med 1997; 38(2):224-231.

31) Gochberg DF, Gore JC. Quantitative magnetization transfer imaging via selective inversion recovery with short repetition times. Magn Reson Med 2007; 57(2):437-441.

32) Bloch, F. Nuclear Induction. Phys Rev 1946; 70:460-474.

33) Mohr PJ, Taylor BN, Newell DB. CODATA recommended values of the fundamental physical constants: 2006. Rev Mod Phys 2008; 80(2):633-730.

34) Du YP, Chu R, Hwang D, Brown MS, Kleinschmidt-DeMasters BK, et al. Fast multislice mapping of the myelin water fraction using multicompartment analysis of T2-star decay at 3T: A preliminary postmortem study. Magn Reson Med 2007; 58(5):865-870.

35) McConnell, HM. Reaction Rates by Nuclear Magnetic Resonance. J Chem Phys 1958; 28:430-431.

36) Kolind SH, Deoni SC. Rapid three-dimensional multicomponent relaxation imaging of the cervical spinal cord. Magn Reson in Med 2011; 65:551-556.

37) Deoni SC, Mercure E, Blasi A, Gasston D, Thomson A, Johnson M, Williams SC, and Murphy DG. Mapping Infant Brain Myelination with Magnetic Resonance Imaging. J Neurosci 2011; 31:784-791.

38) Deoni SCL. Correction of main and transmit magnetic field (B0 and B1) inhomogeneity effects in multicomponent-driven equilibrium single-pulse observation of T1 and T2. Magn Reson Med 2010; 65(4):1021–1035.

39) Scheffler K. Fast frequency mapping with balanced SSFP: Theory and application to proton-resonance frequency shift thermometry. Magn Reson Med 2004; 51(6):1205-1211.

40) Leupold J, Wieben O, Månsson S, Speck O, Scheffler K, et al. Fast chemical shift mapping with multiecho balanced SSFP. Magn Reson Mat in Phys, Bio, and Med 2006; 19(5):267-273.

41) Deoni, SCL. High-resolution T1 mapping of the brain at 3T with driven equilibrium single pulse observation of T1 with high-speed incorporation of RF field inhomogeneities (DESPOT1-HIFI). J Magn Reson Im 2007; 26(4):1106-1111.

42) Carr HY. Steady-state free precession in nuclear magnetic resonance. Phys Rev 1958; 112(5):1693-1701.

43) Santini F, Wetzel SG, Bock J, Markl M, Scheffler K. Time-resolved three-dimensional (3D) phase-contrast (PC) balanced steady-state free precession (bSSFP). Magn Reson Med 2009; 62(4):966-974.

44) Lenz C, Klarhöfer M, Scheffler K. Limitations of rapid myelin water quantification using 3D bSSFP. Magn Reson Mat in Phys, Bio, and Med 2010; 23(3):139-151.

45) Frahm J, Hanicke W, Merboldt KD. Transverse coherence in rapid FLASH NMR imaging. J Magn Reson 1987; 72:307–314.

46) Wood ML, Runge VM. Artifacts due to residual magnetization in three-dimensional magnetic resonance imaging. Med Phys 1988; 15:825–831.

47) Wood ML, Silver M, Runge VM. Optimization of spoiler gradients in FLASH MRI. Magn Reson Imaging 1987; 5:455–463.

48) Wang HZ, Riederer SJ. A spoiling sequence for suppression of residual transverse magnetization. Magn Reson Med 1990; 15:175–191.

49) Crawley AP, Wood MI, Henkelman RM. Elimination of transverse coherences in FLASH MRI. Magn Reson Med 1988; 8:248–260.

50) Zur Y, Wood ML, Neuringer IJ. Spoiling of transverse magnetization in steady-state sequences. Magn Reson Med 1991; 21:251–263.

51) Henkelman RM. Measurement of signal intensities in the presence of noise in MR images. Med Phys 1985; 12(2):232–233.

52) Gudbjartsson H, Patz S. The rician distribution of noisy mri data. Magn Reson Med 1995; 34(6):910–914.

53) Kay SM. Fundamentals of Statistical Signal Processing, Volume I: Estimation Theory (v. 1). 1st ed. Prentice Hall; 1993, p 45.

54) Poor HV. An Introduction to Signal Detection and Estimation (Springer Texts in Electrical Engineering). Springer; 1994, p 175.

55) Zhang F, editor. The Schur Complement and Its Applications (Numerical Methods and Algorithms). 1st ed. Springer; 2005, p 186.

56) Golub GH, van Loan CF. Matrix Computations, 3rd Ed. The Johns Hopkins University Press; 1996, p 81.

57) Bevington P, Robinson DK. Data Reduction and Error Analysis for the Physical Sciences. 3rd ed. McGraw-Hill Science/Engineering/Math; 2002, p 145.

58) Bieri O, Scheffler K. On the origin of apparent low tissue signals in balanced SSFP. Magn Reson Med 2006;56(5):1067–1074.

59) Gloor M, Scheffler K, Bieri O. Quantitative magnetization transfer imaging using balanced SSFP. Magn Reson Med 2008;60(3):691–700.

60) Ou X, Gochberg DF. MT effects and T1 quantification in single-slice spoiled gradient echo imaging. Magn Reson Med 2008;59(4):835–845.

61) Stanisz GJ, Kecojevic A, Bronskill MJ, Henkelman RM. Characterizing white matter with magnetization transfer and T(2). Magn Reson Med 1999;42(6):1128–1136.

62) Crooijmans HJ, Gloor M, Bieri O, Scheffler K. Influence of MT effects on T2 quantification with 3D balanced steady-state free precession imaging. Magn Reson Med 2011;65:195-201.